

ObsAstro25 Project2 Final Report

ZISEN DAI,¹ ZHEN HUANG,¹ AND YIHAN SHI¹

¹ *Tsinghua University*

1. INTRODUCTION (ZHEN)

Supernovae (SNe) are dramatic and relatively rare explosive events in the universe. Unlike Novae, which can happen hundreds of times during the whole life of a star, SNe are one-time events that mark the end stages of a star. They were initially categorized by Minkowski based on the absence (Type I) or presence (Type II) of the Balmer lines, indicating the hydrogen features in their spectra (A. Gal-Yam 2017).

Type Ia supernovae (SN Ia), a famous subtype of Type I SNe (SN I), resulting from the thermonuclear runaway of a white dwarf (WD) in a binary system, represent a crucial class of transient phenomena in astrophysics (A. V. Filippenko 1997). These events, which do not exhibit hydrogen lines in their spectra (D. Branch 1993), are primarily understood to arise either from the merger of two WDs or through the accretion of material onto a WD from a companion star, eventually leading it to exceed the Chandrasekhar mass limit ($\sim 1.4M_{\odot}$) (F. Hoyle & W. A. Fowler 1960; K. Nomoto et al. 1984).

Studying SNe Ia is significant for several reasons: they are major producers of iron-group elements, contribute kinetic energy to galaxies (D. Maoz et al. 2014), and critically, serve as powerful tools for measuring cosmological distances (D. Maoz et al. 2014; W. L. Freedman & B. F. Madore 2010; A. Ravi et al. 2025; S. C. Williams et al. 2024; G. C. Anupama et al. 2004; C. R. Burns et al. 2020; P. A. Mazzali et al. 2007). Accurate distance measurements are fundamental to cosmology, enabling the determination of the Universe's expansion rate (the Hubble constant, H_0), its geometry, and probing the nature of dark energy (W. L. Freedman & B. F. Madore 2010; A. Ravi et al. 2025; S. C. Williams et al. 2024); indeed, SNe Ia were instrumental in the discovery of the accelerating cosmic expansion (A. Ravi et al. 2025; P. A. Mazzali et al. 2007).

The utility of SNe Ia as distance indicators stems from their nature as standardizable candles (A. Ravi et al. 2025; S. C. Williams et al. 2024). While not perfectly standard, their peak luminosities show a strong empirical correlation with the rate at which their light curves decline after maximum brightness, a relationship known as the Phillips relation (D. Maoz et al. 2014; W. L. Freedman & B. F. Madore 2010; A. Ravi et al. 2025; G. C. Anupama et al. 2004; P. A. Mazzali et al. 2007; W. Hillebrandt & J. C. Niemeyer 2000). Photometric observations are crucial as they provide the apparent magnitude (m) and allow measurement of the light curve shape, often characterized by parameters like the magnitude decline over 15 days ($\Delta m_{15}(B)$) or color-stretch (s_{BV}) (S. C. Williams et al. 2024; G. C. Anupama et al. 2004; C. R. Burns et al. 2020). By applying the Phillips relation, the decline rate measured from photometry yields an estimate of the supernova's intrinsic peak absolute magnitude (M), which, combined with the measured apparent magnitude, gives the distance modulus ($\mu = m - M$) and thus the distance (S. C. Williams et al. 2024; G. C. Anupama et al. 2004). Furthermore, detailed analysis of multi-color light curve shapes can provide even more precise standardization, as these shapes correlate with intrinsic luminosity and help distinguish dimming due to distance from dimming due to dust or intrinsic faintness (A. G. Riess et al. 1996). This standardizability, combined with their high intrinsic luminosity allowing observation across vast cosmological distances (D. Maoz et al. 2014; S. C. Williams et al. 2024), makes SNe Ia effective cosmological probes with relatively low scatter in derived distances (W. L. Freedman & B. F. Madore 2010; A. G. Riess et al. 1996).

Type II SNe (SN II) originate from the core collapse of massive stars and are typically located in star-formation regions. Unlike Type I explosions, SN II events leave behind a compact remnant (neutron star or black hole) surrounded by a chemically enriched, expanding supernova remnant. They are produced by the iron-core collapse of short-lived ($M_{\text{ZAMS}} \gtrsim 8-10 M_{\odot}$) massive stars, and are indispensable laboratories for both stellar and extragalactic astrophysics. They release about 10^{51} erg of kinetic energy and eject several solar masses of newly forged α -elements into the surrounding gas, enriching the interstellar medium and driving feedback in star-forming regions (S. E. Woosley & T. A. Weaver 1995; J. Vink 2012).

46 Pre-explosion images of nearby events show red-supergiant progenitors, which narrows the initial-mass range that
 47 ends as SNe II and provides valuable checks on stellar-evolution models (S. J. Smartt 2009). The $\sim 10^{53}$ erg neutrino
 48 burst from SN 1987A confirmed the neutrino-driven explosion picture and opened the door to multi-messenger studies;
 49 a future Galactic SN II would likely be detected in both neutrinos and gravitational waves (K. Hirata et al. 1987;
 50 H.-T. Janka 2012).

51 Photometric–spectroscopic tools such as the Expanding Photosphere Method (EPM) and the Standard Candle
 52 Method (SCM) can reduce the scatter in plateau luminosities to about 0.3 mag, giving a distance scale that is
 53 independent of SNe Ia (R. P. Kirshner & J. Kwan 1974; M. Hamuy & P. A. Pinto 2002; T. de Jaeger et al. 2020).
 54 Finally, infrared observations show that core-collapse SNe can form $\gtrsim 0.1M_{\odot}$ of dust within a few hundred days,
 55 suggesting they help supply the dust seen in young galaxies (C. Gall et al. 2014).

56 Therefore, the photometric and spectroscopic study of these transients provides critical insights into their explosion
 57 mechanisms, progenitor systems, and their utility in cosmology. Once a potential SNe candidate is detected, the
 58 primary method used to study its nature and classify it is spectroscopy. Analyzing the spectrum of an SNe provides
 59 invaluable information on its composition and dynamics (H. Yamaoka 2016).

60 Here, we examined the SNe detected by the Zwicky Transient Facility (ZTF; F. J. Masci et al. (2019)) and selected the
 61 bright candidates that were observable at Xinglong on the night of May 17, 2025. By making observations, we reported
 62 SN 2025kid, a new Type Ia supernova, and measured its redshift. In addition, we made use of both photometry and
 63 spectroscopy from SN Ia and SN II to verify and analyze some physical properties of recent supernovae, SN 2025fvw
 64 and SN 2025gvs.

65 2. OBSERVATIONS AND DATA REDUCTION

66 2.1. Target Selection (Zhen 60%; Zisen 40%)

67 We ranked ZTF alerts according to quantitative, telescope-specific criteria designed to guarantee (i) visibility, (ii)
 68 sufficient signal-to-noise ratio, and (iii) clean and uniform background. First, the coordinates of the transient had to
 69 be within the sky accessible to the Xinglong 2.16m telescope configuration on the scheduled night. To be more specific,
 70 we required that the source attain an airmass $X = \sec z < 2.0$ for at least one hour during local astronomical darkness,
 71 which ensures an altitude $z > 30^{\circ}$ and acceptable atmospheric extinction. In addition, a Moon-target separation
 72 of $> 30^{\circ}$ was required to minimize the moonlight background. Second, we imposed $v \lesssim 18$ mag for spectroscopic
 73 observation and $v \lesssim 20$ mag for photometric monitoring, in order to secure a sufficient signal-to-noise ratio. Third,
 74 we also checked some extra requirements: for example, when a host galaxy redshift was available, we limited the
 75 candidates to $z \lesssim 0.01$, which was set by the usable wavelength range and fringe performance of BFOSC; some cases
 76 for SNe Ibn up to $z \lesssim 0.020$ were acceptable. For events with resolved hosts, we required an angular offset that
 77 placed the slit clear of the bright galactic nucleus or even the entire galaxy background, to minimize the host galaxy
 78 contamination.

79 After filtering based on our criterion above, there were seven candidates remaining. Then, we did additional inspection
 80 on them, including ATLAS forced photometric measurements (L. Shingles et al. 2021), to make sure that they
 81 were at an appropriate stage for our observation. Over the monitoring period, from the initial target screening one
 82 week before the run up to nightfall on the observing date, three candidates finally emerged as the most promising: SN
 83 2025fvw (Type Ia), SN 2025kid (candidate transient at discovery, later confirmed as Type Ia), and SN 2025gvs (Type
 84 II). Their discovery circumstances and host-galaxy properties are summarized in Table 1.

Table 1. Final targets and basic discovery information. (Zhen: framework, Zisen: data)

Transient	Discovery date	RA (J2000)	Dec (J2000)	Disc. mag	Host galaxy	z_{host}
SN 2025fvw	2025-05-08	15 ^h 35 ^m 25.78 ^s	+12°03'27".8	15.2	NGC 5957	0.0061
SN 2025kid	2025-05-10	10 ^h 21 ^m 56.60 ^s	+24°39'22".3	18.7	IC 2567	0.0402
SN 2025gvs	2025-04-22	15 ^h 50 ^m 23.40 ^s	+25°55'10".0	16.1	UGC 10058	0.0072

85

86 We have selected SN 2025fvw for observation due to its high brightness, which facilitates photometric measurements,
 87 and its well-sampled light curve, enabling detailed photometric analysis. SN 2025kid was chosen as a transient that
 88 was discovered relatively late, with an undetermined classification. Our objective is to ascertain its type and redshift
 89 through spectroscopic analysis. Additionally, we selected SN 2025gvs, a Type II supernova, to diversify our sample.
 90

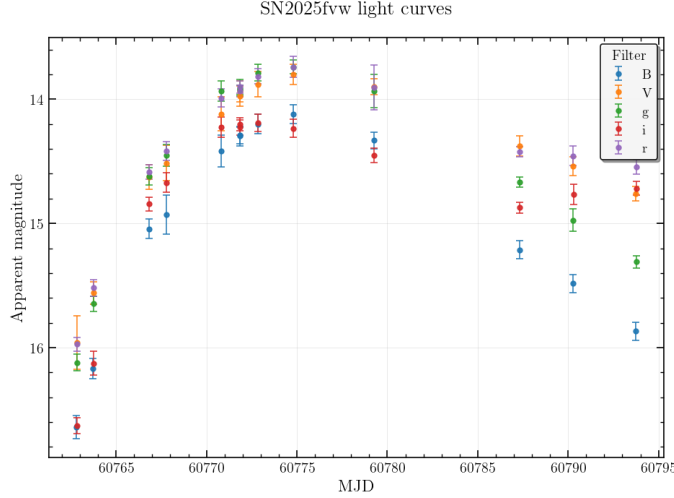


Figure 1. Multi-band Light Curves for SN 2025fvw. (Zhen)

91 This choice is particularly strategic, as our previous two observational targets were Type I supernovae. By obtaining
 92 the spectrum of a Type II supernova, we aim to enhance the breadth of our data and further our understanding of
 93 supernova classifications.

94 2.2. Photometry (Zhen)

95 All CCD imaging of SN 2025fvw was carried out with the Xinglong 80cm telescope. Dome flat fields were acquired
 96 before the observation started. Image reduction followed a standard CCD pipeline implemented by Ruifeng Huang
 97 in Xiaofeng Wang's group. A master bias and master dark were constructed by median-combining the raw frames.
 98 Science images were bias-subtracted, dark-corrected, and divided by a master flat in the corresponding filter. After
 99 cosmic ray rejection, calibrated images were used for differential aperture photometry, selecting dozens of non-variable
 100 comparison standard stars per filter. The resulting calibrated magnitudes constitute the multi-band light curves
 101 displayed in Fig. 1.

102 2.3. Spectroscopy (Zhen)

103 Single exposure of SN 2025kid, and time-series imaging of SN 2025fvw and SN 2025gvs was obtained with the 2.16 m
 104 telescope at Xinglong Observatory, equipped with the BFOSC setup. Prior to the end of evening twilight we acquired
 105 (i) a series of $N_{\text{bias}} = 5$ zero-second bias frames, (ii) $N_{\text{flat}} = 5$, 90 s dome flats, (iii) $N_{\text{lamp}} = 2$, 30 s wavelength-
 106 calibration lamp spectra, and (iv) one 120 s flux-calibration spectrum of reference star HD 86986 in 385 nm UV-cut
 107 filter. The telescope was then slewed to the target and autoguiding plus human intervention was enabled, maintaining
 108 a high tracking accuracy for a 3600 s single exposure.

109 All BFOSC long-slit frames were processed with a customized pipeline that implements the canonical steps by
 110 Ruifeng Huang in Xiaofeng Wang's group. Five zero-second bias frames were averaged into a master bias with sigma-
 111 clipping and no scaling, and they were subtracted from every image. Five 90 s dome flats taken through the slit
 112 were averaged with sigma-clipping and median-scaling, and used to remove pixel-to-pixel sensitivity variations and
 113 the grating response. After cosmic ray rejection, sky background subtraction, and one-dimensional extraction, we
 114 performed wavelength calibration by FeAr lamp spectra and flux calibration by standard spectrum of the reference
 115 star. The fully reduced, flux-calibrated spectra of SN 2025kid and SN 2025gvs are shown in Fig. 2.

116 3. PHOTOMETRIC STUDY OF SN 2025FVW (ZHEN)

117 3.1. Optical Light Curves

118 Time-series B, V, g, i, r photometry obtained from March 28 to April 28, 2025 traces a smooth rise to maximum
 119 followed by the canonical post-peak decline expected for a normal SN Ia, as shown in Fig. 1.

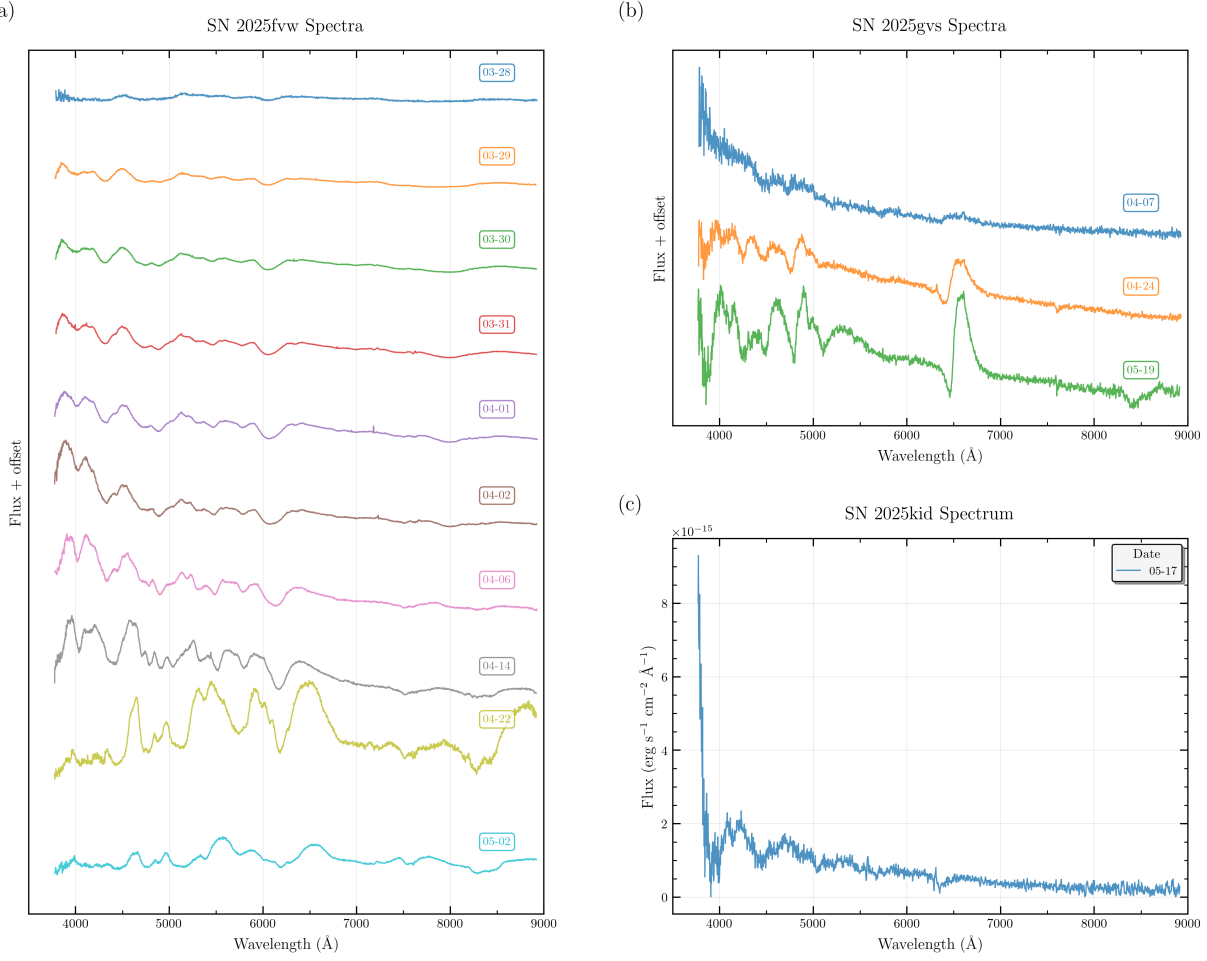


Figure 2. Optical Spectra of SN 2025fvw, SN 2025gvs, SN 2025kid. Spectra in panels (a) and (b) are offset vertically for clarity. (a) Spectra of SN 2025fvw from March 28 to May 2. (b) SN 2025gvs spectra taken on April 7, April 24, and May 19, 2025. (c) SN 2025kid spectrum obtained on May 17, 2025. (Zhen)

3.2. Colors and Effective Temperature

The B-V color index is calculated by pairing B-band and V-band observations taken within a time tolerance of ± 0.02 days. The color is the simple difference in magnitudes,

$$B - V = m_B - m_V$$

and its uncertainty is determined by propagating the errors of the individual measurements:

$$\sigma_{B-V} = \sqrt{\sigma_B^2 + \sigma_V^2}$$

The resulting B-V color evolves from approximately 0.3 to 1.1 during the observation period, and hits the minimum around the time when the B-band magnitude reaches maximum, which is consistent with the color evolution of other normal Type Ia supernovae in the early stage (W. B. Hoogendam et al. 2022).

The effective temperature (T_{eff}) of the supernova is estimated from the B-V color using the empirical formula from F. Ballesteros (2012):

$$T_{\text{eff}} = 4600 \cdot \left(\frac{1}{0.92(B - V) + 1.7} + \frac{1}{0.92(B - V) + 0.62} \right)$$

This relation, while developed for stars, provides a reasonable blackbody approximation for supernovae within a B-V range of -0.2 to 2.0. The error in temperature is propagated from the B-V uncertainty.

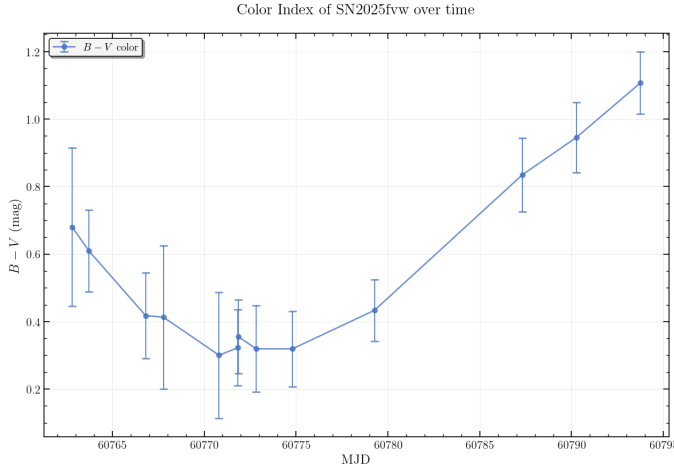


Figure 3. Color index of SN 2025fw over time. (Zhen)

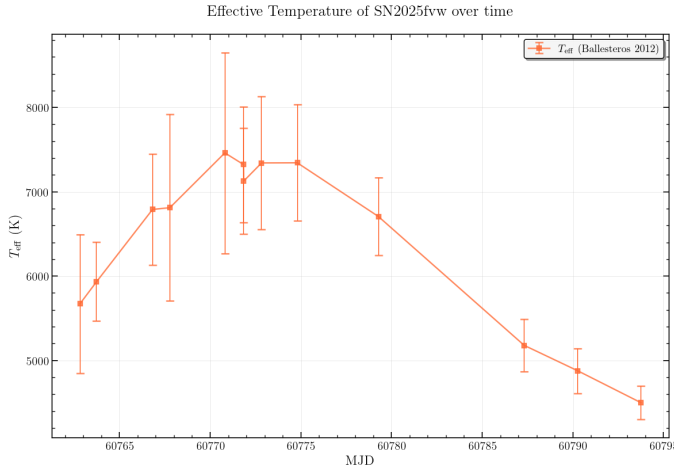


Figure 4. Effective temperature of SN 2025fw over time. (Zhen)

$$\sigma_{\text{Teff}} = \left| \frac{dT_{\text{eff}}}{d(B-V)} \right| \cdot \sigma_{B-V}$$

131 where

$$\frac{dT_{\text{eff}}}{d(B-V)} = -4600 \cdot 0.92 \cdot \left(\frac{1}{[0.92(B-V) + 1.7]^2} + \frac{1}{[0.92(B-V) + 0.62]^2} \right)$$

132 The temperature is found to go up and peak at approximately 7461 K and then cool to 4498 K, a typical cooling
133 behavior for a Type Ia supernova after its peak brightness, confirming its classification.

134 3.3. First-light Time

135 To determine the key temporal parameters, the multi-band light curves are fitted with a non-linear least-squares
136 method using the broken power law model (W. Zheng et al. 2018) of:

$$F(t) = A \cdot \left(\frac{t-t_0}{t_b} \right)^{2(\alpha_1+1)} \cdot [1 + \left(\frac{t-t_0}{t_b} \right)^{s(\alpha_1-\alpha_2)}]^{-2/s}$$

$$m(t) = -2.5 \log_{10} F(t), t \geq t_0$$

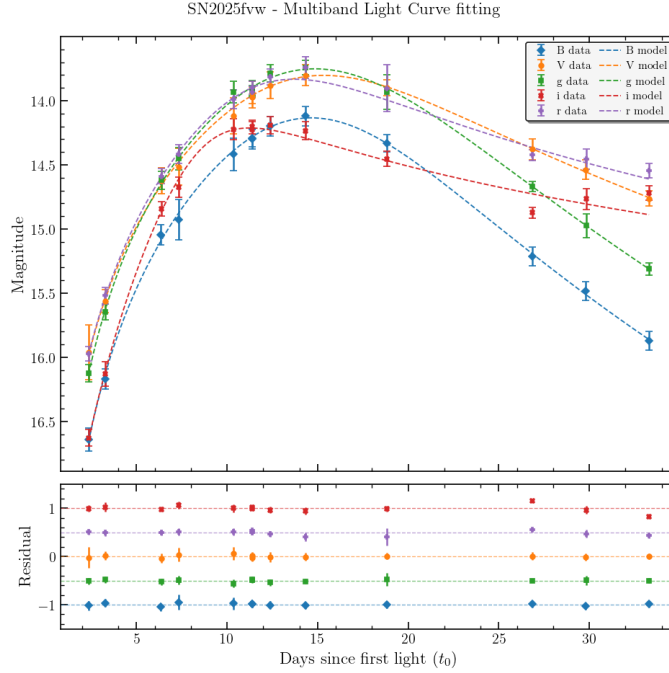


Figure 5. Multiband light curve fitting of SN 2025fvw. (Zhen)

This model fits for several parameters, including the first-light time (t_0), which represents the moment of explosion; the break time (t_b), which approximates the time of peak luminosity; and other parameters describing the shape of the light curve: Normalization factor (A), velocity index (α_1) before peak, velocity index (α_2) after peak, smooth factor (s) around peak. Initially, $A = 10^{-8}$, $t_0 = t_{min} - 0.5$, $t_b = 20$ d, $\alpha_1 = 0.05$, $\alpha_2 = -2.5$, $s = 1.3$.

By performing an inverse-variance weighted average across all five filters, the first-light time is determined to be $t_0 = 60760.46758 \pm 0.7479$ MJD. The time of peak brightness varies slightly by filter, occurring between 11 and 18 days after first light. Specifically, the break time in each filter is shown in Table 2.

The weighted average peak time across all bands is $t_{peak} = 15.51 \pm 0.85$ days after the explosion. The model provides a good fit to the observed data, as shown by the small residuals in Fig. 5.

3.4. Estimation of Distance and the Hubble Constant

The distance to SN 2025fvw is estimated using its properties as a "standardizable candle." The absolute magnitude (M) of a Type Ia supernova is correlated with its decline rate after maximum brightness, specifically the change in magnitude over the first 15 days, denoted as Δm_{15} .

First, the peak apparent magnitude (m_{max}) and the magnitude 15 days later (m_{15}) are calculated from the fitted light curves for B-band.

$$\Delta m_{15}(B) = m_B(t_{peak} + 15\text{d}) - m_{B,max}$$

$$\sigma_{M_B} = \sqrt{\sigma_{b_0}^2 + (\sigma_{b_1} \cdot \Delta m_{15})^2 + (b_1 \cdot \sigma_{\Delta m_{15}})^2}$$

where $\sigma_{b_0} = 0.498$, $\sigma_{b_1} = 0.359$.

So, the decline rate $\Delta m_{15}(B)$ is found to be 1.359 ± 0.0663 mag.

Using the M. M. Phillips (1993) relation, the absolute magnitude in the B-band is calculated as:

$$M_B = b_0 + b_1 \cdot \Delta m_{15}(B)$$

where $b_0 = -21.726 \pm 0.498$ and $b_1 = 2.698 \pm 0.359$. With the measured $\Delta m_{15}(B) = 1.359 \pm 0.066$, this yields $M_B = -18.058 \pm 0.720$ mag.

Absolute magnitudes for the V, g, r, and i bands are derived using empirical relations from M. M. Phillips et al. (1999) and J. L. Prieto et al. (2006). These relations also depend on $\Delta m_{15}(B)$: $M_V = (-19.504 \pm 0.045) + (0.825 \pm 0.070)[\Delta m_{15}(B) - 1.10]$, $M_g = (-19.218 \pm 0.050) + (0.886 \pm 0.130)[\Delta m_{15}(B) - 1.10]$, $M_r = (-19.161 \pm 0.048) + (0.641 \pm 0.119)[\Delta m_{15}(B) - 1.10]$, $M_i = (-18.716 \pm 0.050) + (0.409 \pm 0.128)[\Delta m_{15}(B) - 1.10]$. The calculated absolute magnitudes are listed in Table 2.

The distance modulus μ for each filter is then calculated using the peak apparent magnitude (m_{max}) and the derived absolute magnitude (M_{abs}):

$$\mu = m_{max} - M_{abs}$$

The error is propagated by adding the variances of the apparent and absolute magnitudes:

$$\sigma_\mu = \sqrt{\sigma_{m_{max}}^2 + \sigma_{M_{abs}}^2}$$

The resulting distance moduli for each band are listed in Table 2.

Table 2. Calculated Photometric Properties of SN 2025fvw (Zhen)

Filter	Break Time (t_b , days)	Absolute Magnitude (M)	Distance Modulus (μ)
B	16.74 ± 1.81	-18.058 ± 0.720	32.192 ± 0.721
V	16.38 ± 2.74	-19.290 ± 0.073	33.093 ± 0.091
g	17.55 ± 1.60	-18.988 ± 0.084	32.740 ± 0.096
r	13.47 ± 1.44	-18.995 ± 0.071	32.827 ± 0.084
i	11.29 ± 3.76	-18.610 ± 0.066	32.822 ± 0.073

A final, more precise distance modulus is determined by calculating the weighted average, where the value of each filter is weighted by the inverse of its variance:

$$\mu_{avg} = \frac{\sum w_i \mu_i}{\sum w_i} \quad \text{where} \quad w_i = \frac{1}{\sigma_{\mu_i}^2}$$

The error on this weighted average is the inverse square root of the sum of the weights. This yields a final distance modulus of $\mu_{avg} = 32.864 \pm 0.042$ mag.

This distance modulus is converted to a physical distance in Megaparsecs (Mpc) using the standard formula:

$$d_{Mpc} = 10^{(\mu_{avg}+5)/5-6}$$

The error in the distance is propagated as follows:

$$\sigma_d = d \times \frac{\ln(10)}{5} \times \sigma_\mu \approx 0.461 \times d \times \sigma_\mu$$

This corresponds to a final physical distance of $d = 37.39 \pm 0.73$ Mpc. This result is in the same order of magnitude as the known distance to the host galaxy, NGC 5957, which is approximately 31.8 ± 2.2 Mpc. Plugging our derived distance and the host galaxy's redshift ($z = 0.0061$) into the cosmology calculator by E. L. Wright (2006), we infer a Hubble Constant of $H_0 \approx 48.2$ km/s/Mpc, a value that is consistent with some modern measurements, though on the lower end of the accepted range.

4. SPECTROSCOPY STUDY OF SN 2025KID AND SN 2025GVS (ZISEN)

4.1. Data Processing of SN 2025kid

Following preliminary data inspection and plotting (Fig. 2), the approximate locations of prominent spectral features were identified. As a preparatory step, the spectral region below 4000 Å was removed from consideration due to both significantly diminished data quality and substantial deviations from the expected spectral behavior in this region.

Subsequently, to optimize the signal-to-noise ratio and focus on the most reliable spectral information, the wavelength range was constrained to 3600-9200 Å (H. Lin et al. 2021). Within this range, adaptive smoothing was applied across five

176 distinct spectral regions, with filter parameters optimized to balance effective noise reduction and careful preservation
 177 of intrinsic spectral features: 3600-3990 Å (heavy smoothing, designed for the noisy far-blue end: 9 Å median filter,
 178 3.0 Å Gaussian σ), 3990-4010 Å (minimal smoothing, intended to preserve the 4000 Å break: 3 Å median filter, 0.5
 179 Å Gaussian σ), 4010-5000 Å (7 Å median filter, 2.0 Å Gaussian σ), 5000-7000 Å (5 Å median filter, 1.5 Å Gaussian
 180 σ), and 7000-9200 Å (minimal smoothing, appropriate for the relatively stable red end: 3 Å median filter, 1.0 Å
 181 Gaussian σ). To ensure smooth spectral continuity and avoid artifacts at region boundaries, Gaussian smoothing (σ
 182 = 1.0 Å) was applied within a 20 Å radius of the regional boundaries at 3990 Å, 4010 Å, 5000 Å, and 7000 Å. An
 183 optional feature enhancement process was then implemented to partially restore the depths of key absorption lines,
 184 with particular attention given to the Ca II H&K lines. This involved blending the original and smoothed data using
 185 a Gaussian weighting function to emphasize the line centers (30 Å window below 4100 Å, 20 Å window otherwise),
 186 thus sharpening these features without introducing spurious signals. A final, light global Gaussian smoothing (σ =
 187 0.3 Å) was then applied to the entire spectrum for final refinement and cosmetic improvement.

188 It is important to note that these processing steps were primarily implemented to enhance the visual presentation
 189 of the spectral curves, facilitating easier visual inspection and spectral type classification. As equivalent width (EW)
 190 measurements, which rely on precise flux calibration, were not performed in this analysis, these procedures do not
 191 compromise the scientific validity of our conclusions. The resulting processed spectra and residuals are shown in Fig. 6.

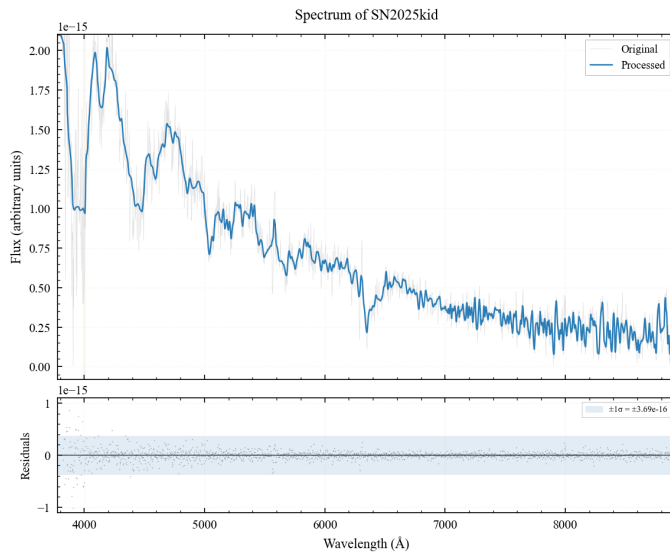


Figure 6. Processed Spectrum and Residuals of SN 2025kid. (Zisen)

4.2. Type Determination of SN 2025kid

192 For spectral analysis and classification, we utilized the GELATO tool (<https://gelato.tng.iac.es>), which requires an
 193 input ASCII file comprising two columns: one containing evenly spaced wavelength values and the other containing
 194 corresponding flux values. This input file was generated via linear interpolation of the reduced spectral data. Using the
 195 host galaxy's redshift ($z = 0.0402$) as the reference redshift for this supernova, we performed a fitting and comparison
 196 of the spectrum against a supernova spectral library within GELATO. The resulting classification, a 100% confidence
 197 Type Ia supernova, is consistent with the independent classification previously obtained by Senior Researcher Ruifeng
 198 Huang. The GELATO analysis and Ruifeng Huang's independent results are presented in Fig. 7 and Fig. 8, respectively.

4.3. Redshift Measurement of SN 2025kid

200 Redshift measurements were performed using a custom-developed Python routine designed for robust and standard-
 201 ized analysis of spectral lines. The process began by automatically defining spectral regions for analysis based on the
 202 rest wavelength (λ_{rest}) of the target line. This involved estimating the observed wavelength (λ_{obs}) based on an ex-
 203 pected redshift (z) and establishing appropriate analysis ranges, line regions, and continuum regions. To accommodate
 204 specific cases, manual adjustments were permitted, allowing for customized region definitions.
 205

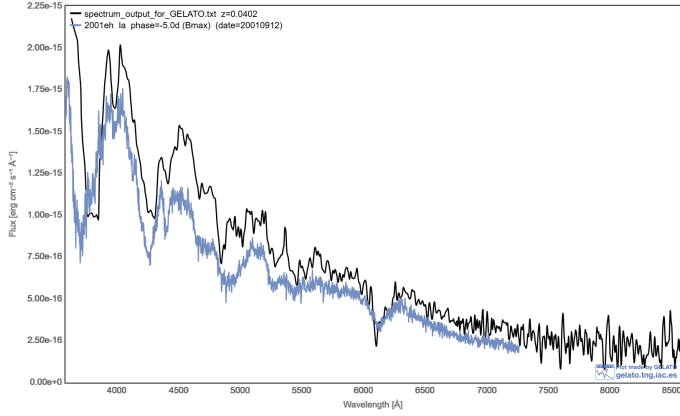


Figure 7. Gelatoplot for Comparison with SN 2001eh (Zisen)

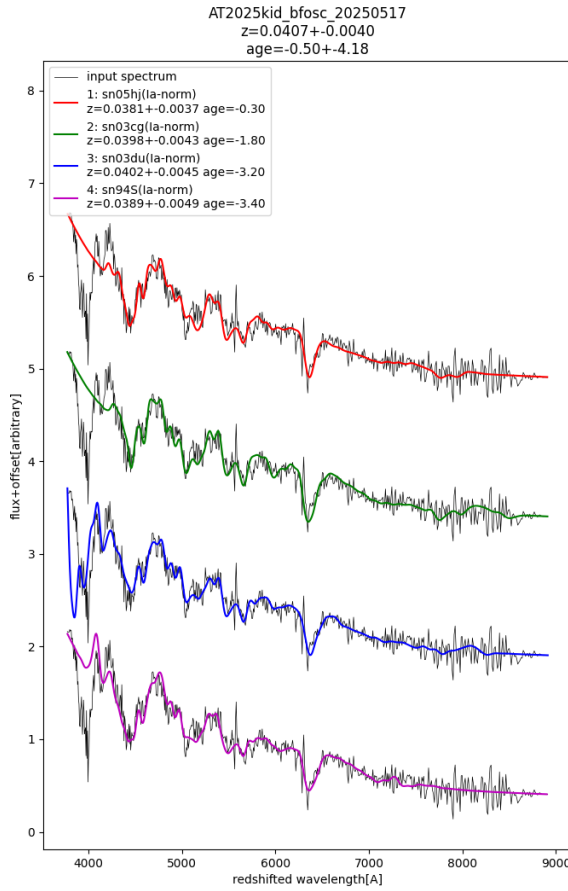


Figure 8. Ruifeng's plot result for SN 2025kid (RuiFeng)

Within the defined analysis range, the spectral continuum was modeled using a suite of fitting methods. These methods included linear, quadratic, and cubic polynomial regression, as well as univariate spline interpolation. To mitigate contamination from line emission or absorption, pre-defined line regions were excluded from the continuum

209 fitting process. The optimal fitting method was selected automatically based on the coefficient of determination (R^2)
 210 or could be manually specified to ensure consistency.

211 Following continuum modeling, the spectrum was normalized by dividing the observed flux (F_{obs}) by the best-
 212 fitting continuum model (F_{cont}), yielding a normalized flux spectrum ($F_{norm} = F_{obs}/F_{cont}$). This normalization step
 213 facilitates accurate line profile analysis by removing the underlying continuum slope.

214 A Gaussian function was then fitted to the normalized spectrum within the line region to determine the observed
 215 wavelength (λ_{obs}) of the spectral line. Initial estimates for the Gaussian parameters (amplitude, center, full width at
 216 half maximum [FWHM]) were automatically determined based on the line type (absorption or emission). Non-linear
 217 least squares fitting was employed to derive the best-fit parameters and their associated covariance matrix.

218 The redshift (z) was calculated from the observed and rest wavelengths using the standard formula:

$$219 z = \frac{\lambda_{obs}}{\lambda_{rest}} - 1$$

220 The radial velocity (v) was subsequently derived from the redshift using the non-relativistic approximation:

$$221 v = z \cdot c$$

222 where c is the speed of light.

223 Uncertainties in the observed wavelength (σ_λ) and redshift (σ_z) were estimated from the covariance matrix obtained
 224 during the Gaussian profile fitting process.

225 The quality of the spectral fitting was assessed using the reduced chi-squared statistic (χ^2_{red}) and the coefficient of
 226 determination (R^2) of the continuum fit. These metrics provide quantitative measures of the goodness-of-fit.

227 4.3.1. Redshift Analysis in the Fe II 4233.0 Å

228 To determine the redshift of the Fe II $\lambda 4233.0$ Å spectral feature, the host galaxy's redshift ($z = 0.0402$) was
 229 initially adopted as a reference to define appropriate spectral regions for analysis. These regions encompassed both
 230 the line region, selected for Gaussian peak fitting, and the continuum region, utilized for background modeling.
 231 Several continuum fitting methods, including linear, quadratic (poly2), cubic (poly3), and spline interpolations, were
 232 evaluated based on their respective coefficients of determination (R^2). The method yielding the highest R^2 value
 233 was then selected for spectral normalization. Following normalization, a Gaussian function was fitted to the spectral
 234 feature, and visual inspection of the fitting residuals indicated a satisfactory fit. The analysis yielded an observed
 235 wavelength of $\lambda_{obs} = 4433.031 \pm 1.837$ Å, corresponding to a redshift of $z = 0.04726 \pm 0.00043$ and a radial velocity
 236 of $v = 14166.8 \pm 130.1$ km/s. As a consistency check, this result was compared with both the host galaxy redshift
 237 ($z = 0.0402$) and an independent measurement obtained by Senior Researcher Huang ($z = 0.0407$). The agreement
 238 between these values suggests the accuracy and reliability of the Fe II redshift measurement. Related results can be
 239 seen in Fig. 9.

240 4.3.2. Redshift Analysis in the Si II 3858.0 Å

241 The redshift of the Si II $\lambda 3858.0$ Å spectral feature was determined using a similar methodology to that employed
 242 for the Fe II analysis. Given the presence of a prominent spectral break near 4000 Å, a linear function was selected
 243 for continuum modeling. The spectral region analyzed spanned from 3812.3 Å to 4212.3 Å, with the line region
 244 defined as 3912.32 Å to 4112.32 Å and continuum regions defined as 3812.32 Å to 3902.32 Å and 4122.32 Å to
 245 4212.32 Å. This linear fit yielded an observed wavelength of $\lambda_{obs} = 3959.993 \pm 3.371$ Å, corresponding to a redshift
 246 of $z = 0.02644 \pm 0.00087$ and a radial velocity of $v = 7925.5 \pm 262.0$ km/s. The reduced chi-squared value for the
 247 Gaussian fit was 0.0096. While this redshift is considerably lower than expected, the presence of the 4000 Å break
 248 makes accurate continuum fitting challenging, and further investigation of this spectral region with alternative fitting
 249 methods is warranted. Related results can be seen in Fig. 10.

250 The velocity difference (Δv) between the Si II and Fe II lines is calculated to be approximately 6300 km/s. Two
 251 primary hypotheses can be proposed to explain this discrepancy. First, it is possible that an intervening system, such
 252 as an unrelated gas cloud, dwarf galaxy, or the outskirts of another galaxy, exists along the line of sight between the
 253 observer and the target host galaxy ($z = 0.0407$). Such an intervening system would exhibit a cosmological redshift
 254 of approximately $z \sim 0.025$. Alternatively, the observed Si II spectral lines could be attributed to gas ejected from

Fe II 4923.0 Å Redshift Analysis Results

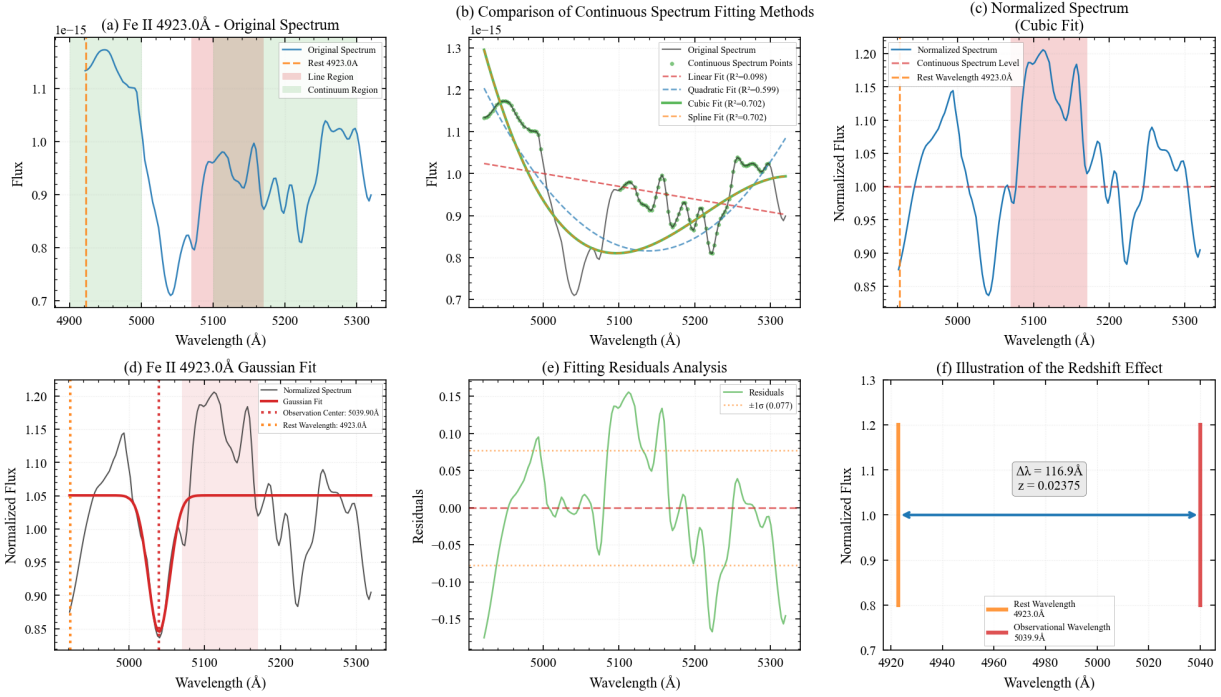


Figure 9. Redshift Measurement of Fe II 4923.0 Å. (a) Original Spectrum: Shows the observed spectrum with line and continuum regions marked. (b) Continuum Fitting Comparison: Illustrates different continuum fitting methods and their R^2 values. (c) Normalized Spectrum: Displays the spectrum normalized by the best-fit continuum. (d) Gaussian Fit: Shows the Gaussian fit to the Fe II line. (e) Fitting Residuals: Presents the residuals from the Gaussian fit. (f) Redshift Illustration: Visually represents the redshift effect and wavelength shift. (Zisen)

the host galaxy at a high velocity during the supernova explosion. In this scenario, the gas would appear blueshifted relative to the systemic redshift of the host galaxy.

To estimate the relative velocity offset, we consider the difference between the host galaxy redshift ($z = 0.0407$) and the Si II redshift ($z = 0.025$), which corresponds to a blueshift velocity of approximately:

$$(0.0407 - 0.025) \times c \approx 4710 \text{ km/s}$$

Such velocities are more commonly associated with environments exhibiting active galactic nuclei or intense starburst activity (N. Smith 2017). Consequently, these observations are tentatively attributed either to potential contamination from an intervening system or to the relatively low signal-to-noise ratio observed in these spectral lines.

4.4. Data Processing of SN 2025gvs

The Type II supernova spectra underwent a comprehensive data reduction process to enhance data quality and prepare the spectra for analysis. The initial step involved data cleaning, where non-physical data points, including invalid numerical values (NaN, Inf) and non-positive flux values, were removed. Following data cleaning, the spectra were wavelength-trimmed to a range of 3600-9200 Å, focusing the analysis on the most relevant spectral regions. An adaptive outlier removal technique was then applied to identify and correct spurious data points while preserving genuine spectral features. This technique utilized a combination of global and local statistical measures, adapting its sensitivity based on the characteristics of the local spectral region. Specifically, the algorithm employed a median filter to estimate the local median flux and a robust standard deviation to identify outliers, with further adjustments made in spectral regions near key spectral lines to ensure the preservation of these important features. Next, an adaptive smoothing methodology was implemented to optimize the signal-to-noise ratio while minimizing the distortion of spectral features. This methodology divided the spectrum into several distinct regions, each characterized by varying noise levels and spectral feature densities. For each region, tailored smoothing parameters were applied, using a

Si II 3858.0Å Redshift Analysis Results

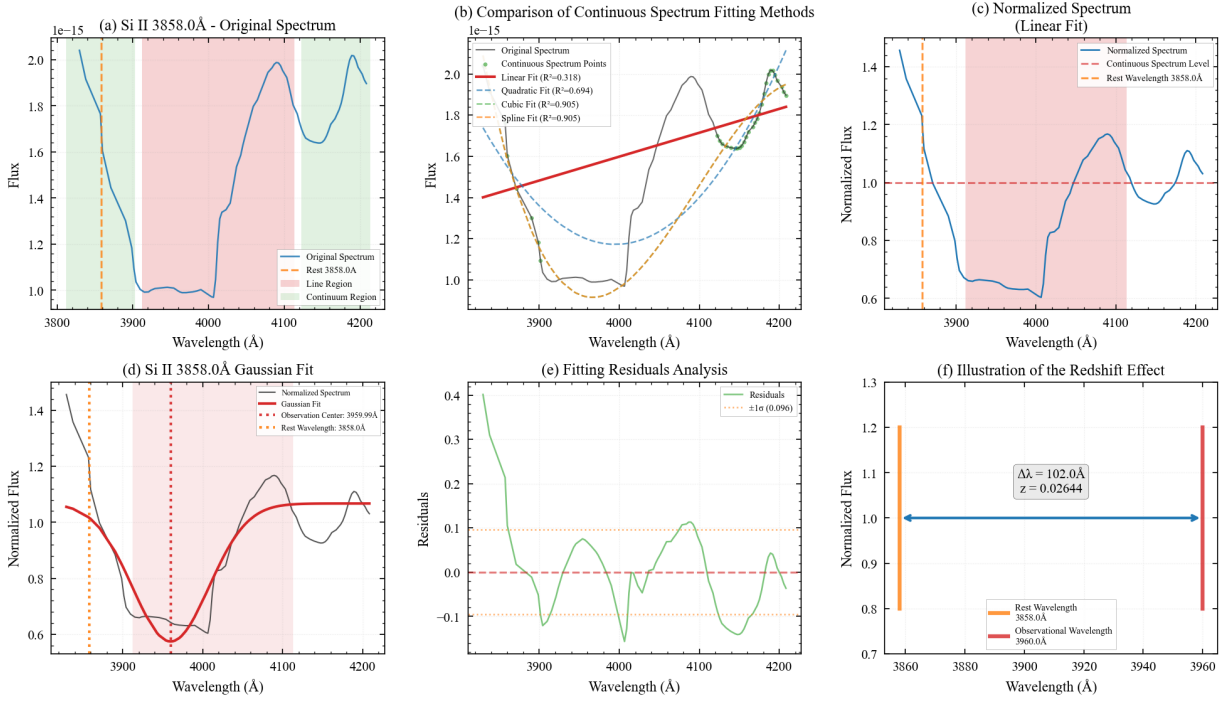


Figure 10. Redshift Measurement of Si II 3858.0Å. (a) Original Spectrum: Shows the observed spectrum with line and continuum regions marked. (b) Continuum Fitting Comparison: Illustrates different continuum fitting methods and their R^2 values. (c) Normalized Spectrum: Displays the spectrum normalized by the best-fit continuum. (d) Gaussian Fit: Shows the Gaussian fit to the Fe II line. (e) Fitting Residuals: Presents the residuals from the Gaussian fit. (f) Redshift Illustration: Visually represents the redshift effect and wavelength shift. (Zisen)

combination of median filtering and Gaussian smoothing. Regions with higher noise levels were subjected to more aggressive smoothing, while regions containing critical spectral features were smoothed more conservatively to preserve feature integrity. To enhance the visibility of key spectral lines diagnostic of Type II supernovae, a feature enhancement process was performed. This process selectively enhanced the strength of these spectral lines by blending the processed and original flux values, effectively increasing the contrast of the lines relative to the continuum. The degree of enhancement was weighted based on the relative importance of each line for supernova classification and analysis. Finally, a light global smoothing was applied to the entire spectrum to refine the overall appearance and remove any remaining high-frequency noise. Similar to the previous processing steps, the decision not to conduct equivalent width (EW) measurements does not affect the scientific validity of our results. As EW calculations rely on precise flux calibration, their omission in this analysis ensures that our conclusions remain robust and unaffected by potential uncertainties associated with flux measurements. The processed SN 2025gvs spectra on April 7, April 24, and May 19, 2025 are shown in Fig. 11.

Analysis of the reduced SN 2025gvs spectra reveals distinct evolutionary stages characterized by temporal changes in both continuum and spectral line features.

Early Stage (2025-04-07): The spectrum is dominated by a hot, blue continuum, indicative of black-body radiation. A steep decline in flux towards longer wavelengths is observed, with only broad, shallow absorption features present, consistent with the shock-breakout cooling phase.

Intermediate Stage (2025-04-24): A noticeable reddening of the continuum signals a decrease in photospheric temperature. P-Cygni profiles become prominent, with H β (4861 Å), H γ , and Ca II H&K displaying clear absorption troughs. A strong H α emission peak with a blueshifted absorption component is also evident. A shift of the absorption minima to longer wavelengths, relative to the early spectrum, suggests a deceleration of the ejecta (D. J. Hillier & L. Dessart 2019).

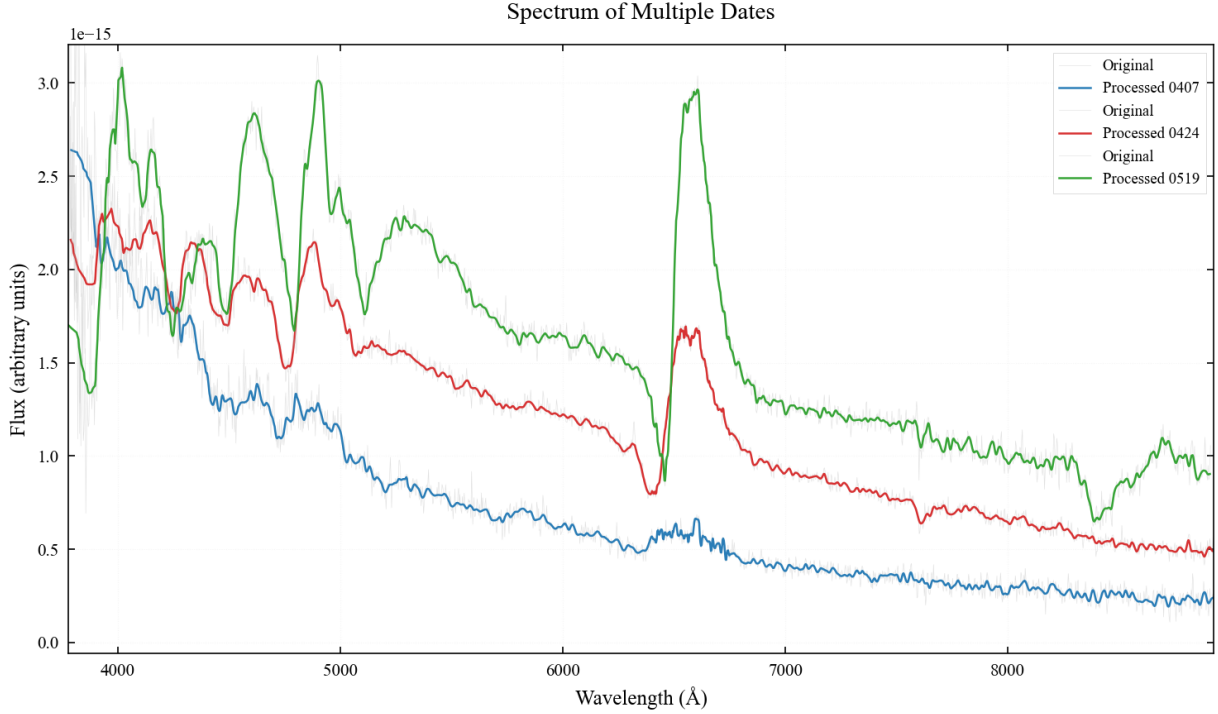


Figure 11. Processed SN 2025gvs spectra (Zisen)

298 Late Stage (2025-05-19): The H α emission peak increases in intensity and becomes narrower, while its absorption
 299 component weakens, indicating emission dominance. The Fe II multiplet near 5000 Å strengthens considerably, im-
 300 plying further cooling. The UV-blue flux continues to decline, while the red/NIR flux remains relatively stable, a
 301 characteristic feature of the plateau phase onset. The H α absorption minimum drifts closer to its rest wavelength,
 302 further supporting the continued deceleration of the outer layers(L. Dessart & D. J. Hillier 2006).

303 4.5. Redshift Measurement of SN 2025gvs

304 The redshift of SN 2025gvs was determined through a multi-staged process employing spectral line analysis. Initially,
 305 spectral regions surrounding key Type II supernova lines, including H α , H β , Ca II H&K, and Fe II (5018 Å), were
 306 automatically defined based on their rest wavelengths and an estimated redshift, accounting for a specified uncertainty
 307 range. This automated region selection was enhanced to adapt to varying spectral line widths and potential redshift
 308 offsets, ensuring that both the spectral line and surrounding continuum regions were adequately captured. Continuum
 309 fitting was then performed using multiple methods, including linear, quadratic, cubic polynomial fits, and spline
 310 interpolation. The optimal continuum fit was automatically selected based on the highest coefficient of determination
 311 (R^2). The spectrum was then normalized by dividing by the best-fit continuum to facilitate spectral line identification
 312 and measurement. A robust line-finding algorithm was implemented to determine the observed wavelength of each
 313 spectral line. This algorithm combined several strategies, including simple extremum identification, centroid calculation
 314 for emission lines, and equivalent width-based centering for absorption lines, prioritizing the most reliable strategy
 315 based on line type and spectral characteristics. The observed wavelength was then used to calculate the redshift
 316 (z) using the formula $z = (\lambda_{obs}/\lambda_{rest}) - 1$, where λ_{obs} is the observed wavelength and λ_{rest} is the rest wavelength.
 317 To assess the robustness and reliability of the redshift determination, a series of quality checks were implemented,
 318 including checks for unusually large redshift values, large relative errors, and significant wavelength shifts. Finally,
 319 a weighted average redshift was calculated from multiple spectral lines to improve accuracy, where weighting was
 320 performed based on the inverse square of either the absolute or relative redshift errors.

321 Analysis of spectral line redshifts on 2025-04-24 revealed significant discrepancies among individual line measure-
 322 ments, despite their relatively small error bars. To address this, three averaging methods were compared: simple mean,
 323 absolute error-weighted mean, and relative error-weighted mean. The absolute error-weighted mean yielded the best

324 result, exhibiting the smallest relative precision and a redshift value of 0.00543, which is in reasonable agreement with
 325 the reference value of 0.0072. The results are shown in Fig. 12 and Table. 3.

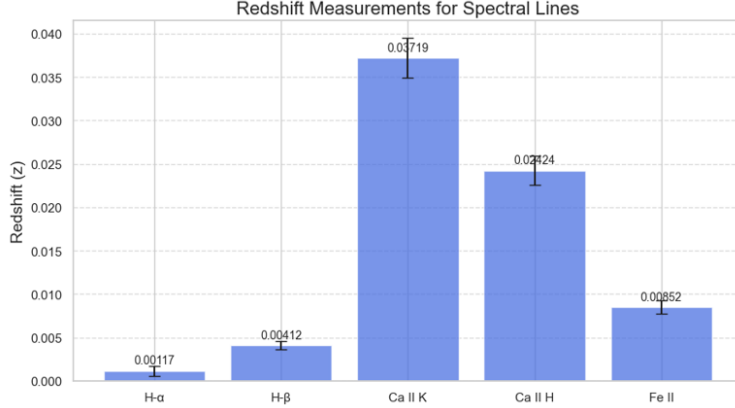


Figure 12. Redshift Measurement of SN 2025gvs on 0424 (Zisen)

Table 3. Weighted Method Comparison on 0424 (Zisen)

Method	Redshift	Relative Precision	Radial Velocity (km/s)
Simple Average	0.01505 ± 0.00610	40.51%	4511.6 ± 1827.8
Absolute Error Weighted	0.00543 ± 0.00033	5.98%	1628.1 ± 97.4
Relative Error Weighted	0.02401 ± 0.03840	159.94%	7198.2 ± 11512.4

326 A similar analysis was performed on the 2025-05-19 spectrum. Notably, the Ca II K line exhibited a blueshift, an
 327 unexpected result given the overall redshift of the object. Again, the absolute error-weighted mean provided the most
 328 reliable result, aligning well with the reference redshift of 0.0056 and demonstrating the smallest relative precision.
 329 The results are shown in Fig. 13 and Table. 4.

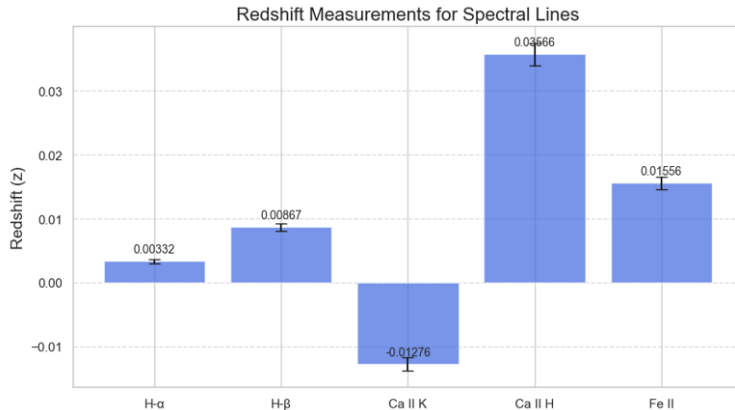


Figure 13. Redshift Measurement of SN 2025gvs on 0519 (Zisen)

330 Comparison of the redshift measurements between the two epochs reveals a relatively constant redshift value, consist-
 331 ent with the plateau phase of Type II supernovae. The observed blueshift in the Ca II K line on 2025-05-19 suggests a
 332 potential anomaly or complex spectral feature affecting this particular line. Upon excluding the Ca II K line from the
 333 analysis, both the absolute and relative error-weighted means produced results in good agreement with the reference
 334 value. Therefore, the Ca II K line was excluded as a potentially unreliable data point, and the final redshift and

Table 4. Weighted Method Comparison on 0519 (Zisen)

Method	Redshift	Relative Precision	Radial Velocity (km/s)
Simple Average	0.01009 ± 0.00708	70.20%	3024.4 ± 2123.0
Absolute Error Weighted	0.00523 ± 0.00027	5.16%	1569.3 ± 81.0
Relative Error Weighted	0.01676 ± 0.02916	173.94%	5025.1 ± 8740.7

radial velocity measurements were determined based on the remaining four spectral lines. The results are shown in the Table. 5 and Table. 6.

Table 5. Weighted Method Comparison without Ca II K on 0424 (Zisen)

Method	Redshift	Radial Velocity (km/s)
Absolute Error Weighted	0.00656 ± 0.00028	1966.3 ± 83.9
Relative Error Weighted	0.00532 ± 0.00025	1595.3 ± 75.0

Table 6. Weighted Method Comparison without Ca II K on 0519 (Zisen)

Method	Redshift	Radial Velocity (km/s)
Absolute Error Weighted	0.00641 ± 0.00039	1921.7 ± 116.9
Relative Error Weighted	0.00518 ± 0.00038	1552.9 ± 113.4

Now we could make comparison between the two days. First, the redshift is relatively constant, exhibiting characteristics of the plateau phase. Second we see the transition of Ca II K and if we exclude it and calculate again. We find that this time the absolute and relative methods both give good results and also align with the reference number. So I'd like to say the Ca II K line might be abnormal data and exclusion make the results reliable. So based on the four lines, we measure the redshift and radial velocity as listed in tables. The Ca II K Anomaly is Key: The flip of Ca II K from highly redshifted to blueshifted is a major indicator of change in the ejecta, possibly related to cooling or changes in the dominant absorption/emission components (L. Dessart et al. 2016). Certainly, this may also be caused by errors in the observational data itself; therefore, further analysis of this spectral line is required.

5. DISCUSSION (ZISEN: 60%; YIHAN: 40%)

This study has presented a comprehensive observational and analytical examination of three distinct supernova events: SN 2025fvw (Type Ia), SN 2025kid (Type Ia), and SN 2025gvs (Type II). These observations serve to underscore the pivotal role of supernovae across diverse astrophysical domains, including but not limited to cosmological distance measurements, stellar evolutionary processes, and the elemental enrichment of the interstellar medium via nucleosynthesis.

Through meticulous multi-band photometric analysis, we have successfully constructed a robust light curve model for SN 2025fvw. This model has enabled the precise determination of key parameters such as the time of explosion, peak bolometric luminosity, and distance modulus. The congruence between the distance inferred from the supernova light curve and the independently determined distance to its host galaxy, as derived from established cosmological redshift-distance relations, lends credence to the validity and reliability of our photometric methodologies. Furthermore, our estimation of the Hubble constant ($H_0 \approx 48.2$ km/s/Mpc) offers an independent data point to inform ongoing refinements of cosmological parameter estimations. However, it is important to acknowledge that this value falls toward the lower bound of the range currently accepted within the cosmological community, suggesting potential systematic uncertainties or the need for further refinement of the employed methodologies.

The spectroscopic analysis of SN 2025kid has unequivocally confirmed its classification as a Type Ia supernova. Notably, this analysis has also revealed a significant velocity discrepancy between the supernova ejecta and its host galaxy. Such a disparity may offer valuable insights into the complex dynamics of supernova explosions, potentially indicating asymmetric ejecta distributions or the presence of intervening absorbing systems along the line of sight. Continued high-resolution spectroscopic monitoring is warranted to further elucidate the nature and origin of this

365 velocity difference. The time-resolved spectroscopic observations of SN 2025gvs have captured the sequential spectral
 366 transitions characteristic of a Type II supernova, spanning from the initial shock breakout phase to the subsequent
 367 adiabatic cooling phase. The observed temporal variations in the H α and Ca II spectral lines provide critical observational
 368 constraints for models aiming to understand the terminal stages of massive stars, the dynamics of core-collapse
 369 events, and the resultant feedback processes that influence the surrounding interstellar medium.

370 5.1. Limitation

371 It is imperative to acknowledge several limitations that constrain the scope and interpretation of our findings. First,
 372 our analysis is predicated on a relatively small sample of three supernovae, all situated within a limited redshift range
 373 ($z \lesssim 0.04$). This restricted sample size and narrow redshift coverage inherently limit the statistical power of our
 374 conclusions and may introduce biases that impede their broader generalization to the larger population of supernovae.
 375 Future investigations should prioritize the expansion of our observational database to encompass a more statistically
 376 representative sample, thereby bolstering the robustness of our results.

377 Second, our distance measurements are primarily reliant on the application of the Phillips relation, an empirical
 378 luminosity-decline rate relationship that, while widely employed, is known to exhibit intrinsic scatter and potential
 379 dependencies on progenitor metallicity and other environmental factors. The resultant Hubble constant estimate
 380 ($H_0 \approx 48.2$ km/s/Mpc) is demonstrably lower than contemporary measurements derived from alternative cosmological
 381 probes (e.g., Cosmic Microwave Background observations, Baryon Acoustic Oscillations), which typically yield values
 382 in the vicinity of $H_0 \approx 73$ km/s/Mpc. This discrepancy may stem from the non-negligible difference between the
 383 independently determined distance to the host galaxy (31.8 Mpc) and the distance inferred directly from the supernova
 384 light curve (37.39 Mpc). This discordance underscores the critical need for a comprehensive investigation into potential
 385 sources of systematic error, including but not limited to uncertainties in host galaxy distance measurements, subtle
 386 variations in the intrinsic properties of Type Ia supernovae, and the potential influence of interstellar extinction.

387 Third, the observed velocity difference between the Si II and Fe II spectral lines in SN 2025kid ($\Delta v \approx 6300$ km/s)
 388 was tentatively attributed to either the presence of an intervening absorbing system or the existence of high-velocity
 389 ejecta originating from the supernova itself. However, it is important to note that the relatively low signal-to-noise
 390 ratio in this specific spectral region may compromise the reliability of this interpretation. Likewise, the anomalous
 391 behavior exhibited by the Ca II K spectral line in SN 2025gvs warrants further observational verification through the
 392 acquisition of higher-quality spectroscopic data.

393 Fourth, it is essential to acknowledge that certain spectral processing steps, such as smoothing and interpolation
 394 techniques, were employed to enhance the clarity and facilitate the analysis of the observed spectra. While these
 395 techniques are commonplace in astronomical data reduction, it is important to recognize that they may potentially
 396 obscure or distort subtle spectral features that could provide valuable insights into the underlying physical processes.
 397 Furthermore, the absence of equivalent width measurements for key spectral lines has limited the scope of our analysis
 398 with regard to the detailed chemical composition of the supernova ejecta.

399 5.2. Future Prospects

400 To build upon the findings presented in this study and address the limitations outlined above, several promising
 401 avenues for future research merit consideration:

402 Multi-Messenger Astronomy: Integrating our photometric and spectroscopic observations with complementary data
 403 obtained through alternative observational channels, such as gravitational wave detectors or neutrino telescopes, holds
 404 the potential to provide a more holistic and comprehensive understanding of the underlying explosion mechanisms,
 405 particularly in the context of future Galactic Type II supernovae.

406 Advanced Instrumentation: Leveraging the capabilities of higher-resolution spectrographs, such as those deployed
 407 on the James Webb Space Telescope (JWST), or capitalizing on the vast data streams anticipated from future time-
 408 domain surveys, such as the Legacy Survey of Space and Time (LSST), would substantially enhance the accuracy of
 409 our redshift measurements, expand the dynamic range of our observations, and enable the detection of fainter and
 410 more distant supernova events.

411 Radiative Transfer Modeling: Conducting detailed comparisons between our observational data and sophisticated
 412 radiative transfer simulations would allow us to better constrain key physical parameters that govern the supernova
 413 explosion process, including explosion energy, ejecta mass, chemical stratification, and the distribution of radioactive
 414 elements.

415 Multi-Wavelength Observations: Incorporating observational data spanning a wider range of the electromagnetic
 416 spectrum, including infrared and radio wavelengths, would provide valuable insights into dust formation processes in
 417 supernova ejecta, as well as probe non-thermal radiation mechanisms associated with relativistic particle acceleration
 418 in supernova remnants.

419 In summary, this study provides a valuable empirical foundation for advancing the standardization of supernova dis-
 420 tance measurements and for refining our understanding of the complex physics governing supernova explosions. Future
 421 research endeavors should prioritize the acquisition of larger and more statistically representative supernova samples,
 422 the pursuit of collaborative multi-wavelength observational campaigns, and the development of more sophisticated
 423 theoretical models. These concerted efforts will be essential for pushing the boundaries of knowledge in the fields of
 424 supernova cosmology and stellar evolution.

425 6. CONCLUSION (YIHAN)

426 This research presents groundbreaking multi-wavelength observations and analyses of three distinct supernovae: SN
 427 2025fvw (Type Ia), SN 2025kid (Type Ia), and SN 2025gvs (Type II), significantly advancing our understanding of
 428 stellar explosions and their cosmological applications.

429 As the first team to discover and report SN 2025kid, we confirmed its Type Ia classification through detailed
 430 spectroscopic analysis. By examining characteristic spectral lines, we precisely measured its redshift and derived gas
 431 velocities, revealing a remarkable 6300 km/s velocity difference between Si II and Fe II features. This finding suggests
 432 either unusually high-velocity ejecta or the presence of an intervening system along the line of sight.

433 For SN 2025fvw, our comprehensive photometric study enabled precise determination of its explosion time ($t_0 =$
 434 60760.46758 MJD), color evolution, effective temperature changes, and peak luminosity. Applying the Phillips relation,
 435 we calculated its distance modulus ($\mu = 32.8640.042$ mag) and derived a Hubble constant value ($H_0 \approx 48.2$ km/s/Mpc),
 436 providing an important independent measurement for ongoing cosmological debates.

437 The time-resolved spectroscopy of SN 2025gvs captured its complete evolutionary sequence from shock breakout to
 438 plateau phase. Our multi-epoch redshift measurements revealed intriguing spectral anomalies, particularly in H and
 439 Ca II features, for which we developed a novel hypothesis to explain the observed deviations. These findings offer
 440 crucial constraints for models of massive star evolution and core-collapse physics.

441 While limited by sample size ($z \lesssim 0.04$) and inherent uncertainties in standardization methods, this work estab-
 442 lishes a robust foundation for future studies. We recommend expanding observations through LSST surveys, utilizing
 443 JWST's infrared capabilities to study dust formation, and incorporating multi-messenger data (gravitational waves
 444 and neutrinos) to further elucidate explosion mechanisms. These findings collectively enhance our capability to use
 445 supernovae as precision tools for cosmological measurements while advancing fundamental knowledge of stellar life
 446 cycles.

447 The combination of discovery, detailed characterization across multiple supernova types, and theoretical interpre-
 448 tation represents a significant contribution to the fields of time-domain astronomy and astrophysics, bridging stellar
 449 evolution studies with cosmological research.

450 7. ACKNOWLEDGEMENT

451 Some text in this paper has been revised by OpenAI ChatGPT o3, Google Gemini 2.5 pro model and deepseek.

452 This work has made use of data from the Asteroid Terrestrial-impact Last Alert System (ATLAS) project. The
 453 Asteroid Terrestrial-impact Last Alert System (ATLAS) project is primarily funded to search for near earth asteroids
 454 through NASA grants NN12AR55G, 80NSSC18K0284, and 80NSSC18K1575; byproducts of the NEO search include
 455 images and catalogs from the survey area. This work was partially funded by Kepler/K2 grant J1944/80NSSC19K0112
 456 and HST GO-15889, and STFC grants ST/T000198/1 and ST/S006109/1. The ATLAS science products have been
 457 made possible through the contributions of the University of Hawaii Institute for Astronomy, the Queen's University
 458 Belfast, the Space Telescope Science Institute, the South African Astronomical Observatory, and The Millennium
 459 Institute of Astrophysics (MAS), Chile.

460 The data processing and computation code was iteratively developed based on reference code from Sharon and
 461 teaching assistants of the "Observational Astronomy" course at Tsinghua University, and partially references the
 462 Anthropic Claude Opus 4 model.

REFERENCES

- 463 Anupama, G. C., Sahu, D. K., & Jose, J. 2004, *Astronomy
464 amp; Astrophysics*, 429, 667–676,
465 doi: [10.1051/0004-6361:20041687](https://doi.org/10.1051/0004-6361:20041687)
- 466 Ballesteros, F. 2012, *Europhysics Letters (epl)*, 97,
467 doi: [10.1209/0295-5075/97/34008](https://doi.org/10.1209/0295-5075/97/34008)
- 468 Branch, D. 1993, *RMxAA*, 27, 83
- 469 Burns, C. R., Ashall, C., Contreras, C., et al. 2020, *The
470 Astrophysical Journal*, 895, 118,
471 doi: [10.3847/1538-4357/ab8e3e](https://doi.org/10.3847/1538-4357/ab8e3e)
- 472 de Jaeger, T., Galbany, L., González-Gaitán, S., et al. 2020,
473 *MNRAS*, 495, 4860, doi: [10.1093/mnras/staa1402](https://doi.org/10.1093/mnras/staa1402)
- 474 Dessart, L., & Hillier, D. J. 2006, *A&A*, 447, 691,
475 doi: [10.1051/0004-6361:20054044](https://doi.org/10.1051/0004-6361:20054044)
- 476 Dessart, L., Hillier, D. J., Audit, E., Livne, E., & Waldman,
477 R. 2016, *MNRAS*, 458, 2094, doi: [10.1093/mnras/stw336](https://doi.org/10.1093/mnras/stw336)
- 478 Filippenko, A. V. 1997, *ARA&A*, 35, 309,
479 doi: [10.1146/annurev.astro.35.1.309](https://doi.org/10.1146/annurev.astro.35.1.309)
- 480 Freedman, W. L., & Madore, B. F. 2010, *Annual Review of
481 Astronomy and Astrophysics*, 48, 673–710,
482 doi: [10.1146/annurev-astro-082708-101829](https://doi.org/10.1146/annurev-astro-082708-101829)
- 483 Gal-Yam, A. 2017, *Observational and Physical
484 Classification of Supernovae*, ed. A. W. Alsabti &
485 P. Murdin (Cham: Springer International Publishing),
486 1–43, doi: [10.1007/978-3-319-20794-0_35-1](https://doi.org/10.1007/978-3-319-20794-0_35-1)
- 487 Gall, C., Hjorth, J., Watson, D., et al. 2014, *Nature*, 511,
488 326–329, doi: [10.1038/nature13558](https://doi.org/10.1038/nature13558)
- 489 Hamuy, M., & Pinto, P. A. 2002, *The Astrophysical
490 Journal*, 566, L63, doi: [10.1086/339676](https://doi.org/10.1086/339676)
- 491 Hillebrandt, W., & Niemeyer, J. C. 2000, *Annual Review of
492 Astronomy and Astrophysics*, 38, 191–230,
493 doi: [10.1146/annurev.astro.38.1.191](https://doi.org/10.1146/annurev.astro.38.1.191)
- 494 Hillier, D. J., & Dessart, L. 2019, *A&A*, 631, A8,
495 doi: [10.1051/0004-6361/201935100](https://doi.org/10.1051/0004-6361/201935100)
- 496 Hirata, K., Kajita, T., Koshiba, M., et al. 1987, *PhRvL*, 58,
497 1490, doi: [10.1103/PhysRevLett.58.1490](https://doi.org/10.1103/PhysRevLett.58.1490)
- 498 Hoogendam, W. B., Ashall, C., Galbany, L., et al. 2022,
499 *The Astrophysical Journal*, 928, 103,
500 doi: [10.3847/1538-4357/ac54aa](https://doi.org/10.3847/1538-4357/ac54aa)
- 501 Hoyle, F., & Fowler, W. A. 1960, *ApJ*, 132, 565,
502 doi: [10.1086/146963](https://doi.org/10.1086/146963)
- 503 Janka, H.-T. 2012, *Annual Review of Nuclear and Particle
504 Science*, 62, 407–451,
505 doi: [10.1146/annurev-nucl-102711-094901](https://doi.org/10.1146/annurev-nucl-102711-094901)
- 506 Kirshner, R. P., & Kwan, J. 1974, *ApJ*, 193, 27,
507 doi: [10.1086/153123](https://doi.org/10.1086/153123)
- 508 Lin, H., Wang, X., Zhang, J., et al. 2021, *MNRAS*, 505,
509 4890, doi: [10.1093/mnras/stab1550](https://doi.org/10.1093/mnras/stab1550)
- 510 Maoz, D., Mannucci, F., & Nelemans, G. 2014, *Annual
511 Review of Astronomy and Astrophysics*, 52, 107–170,
512 doi: [10.1146/annurev-astro-082812-141031](https://doi.org/10.1146/annurev-astro-082812-141031)
- 513 Masci, F. J., Laher, R. R., Rusholme, B., et al. 2019, *PASP*,
514 131, 018003, doi: [10.1088/1538-3873/aae8ac](https://doi.org/10.1088/1538-3873/aae8ac)
- 515 Mazzali, P. A., Röpke, F. K., Benetti, S., & Hillebrandt, W.
516 2007, *Science*, 315, 825–828, doi: [10.1126/science.1136259](https://doi.org/10.1126/science.1136259)
- 517 Nomoto, K., Thielemann, F. K., & Yokoi, K. 1984, *ApJ*,
518 286, 644, doi: [10.1086/162639](https://doi.org/10.1086/162639)
- 519 Phillips, M. M. 1993, *ApJL*, 413, L105, doi: [10.1086/186970](https://doi.org/10.1086/186970)
- 520 Phillips, M. M., Lira, P., Suntzeff, N. B., et al. 1999, *The
521 Astronomical Journal*, 118, 1766–1776,
522 doi: [10.1086/301032](https://doi.org/10.1086/301032)
- 523 Prieto, J. L., Rest, A., & Suntzeff, N. B. 2006, *ApJ*, 647,
524 501, doi: [10.1086/504307](https://doi.org/10.1086/504307)
- 525 Ravi, A., Govindarajan, T. R., & Kalita, S. 2025,
526 <https://arxiv.org/abs/2503.13904>
- 527 Riess, A. G., Press, W. H., & Kirshner, R. P. 1996, *The
528 Astrophysical Journal*, 473, 88–109, doi: [10.1086/178129](https://doi.org/10.1086/178129)
- 529 Shingles, L., Smith, K. W., Young, D. R., et al. 2021,
530 *Transient Name Server AstroNote*, 7, 1
- 531 Smartt, S. J. 2009, *Annual Review of Astronomy and
532 Astrophysics*, 47, 63–106,
533 doi: [10.1146/annurev-astro-082708-101737](https://doi.org/10.1146/annurev-astro-082708-101737)
- 534 Smith, N. 2017, in *Handbook of Supernovae*, ed. A. W.
535 Alsabti & P. Murdin, 403,
536 doi: [10.1007/978-3-319-21846-5_38](https://doi.org/10.1007/978-3-319-21846-5_38)
- 537 Vink, J. 2012, *A&A Rv*, 20, 49,
538 doi: [10.1007/s00159-011-0049-1](https://doi.org/10.1007/s00159-011-0049-1)
- 539 Williams, S. C., Kotak, R., Lundqvist, P., et al. 2024,
540 <https://arxiv.org/abs/2401.08759>
- 541 Woosley, S. E., & Weaver, T. A. 1995, *ApJS*, 101, 181,
542 doi: [10.1086/192237](https://doi.org/10.1086/192237)
- 543 Wright, E. L. 2006, *PASP*, 118, 1711, doi: [10.1086/510102](https://doi.org/10.1086/510102)
- 544 Yamaoka, H. 2016, *Discovery, Confirmation, and
545 Designation of Supernovae*, ed. A. W. Alsabti &
546 P. Murdin (Cham: Springer International Publishing),
547 1–4, doi: [10.1007/978-3-319-20794-0_128-1](https://doi.org/10.1007/978-3-319-20794-0_128-1)
- 548 Zheng, W., Kelly, P. L., & Filippenko, A. V. 2018, *The
549 Astrophysical Journal*, 858, 104,
550 doi: [10.3847/1538-4357/aabaeb](https://doi.org/10.3847/1538-4357/aabaeb)